

Leaky Wave Antenna-Equipped RF Chipless Tags for Orientation Estimation

Onel L. A. López, *Senior Member, IEEE*, Zhu Han, *Fellow, IEEE*, and Ashutosh Sabharwal, *Fellow, IEEE*

Abstract—Accurate orientation estimation of an object in a scene is critical in robotics, aerospace, augmented reality, and medicine, as it supports scene understanding. This paper introduces a novel orientation estimation approach leveraging radio frequency (RF) sensing technology and leaky-wave antennas (LWAs). Specifically, we propose a framework for a radar system to estimate the orientation of a *dumb* LWA-equipped backscattering tag, marking the first exploration of this method in the literature. Our contributions include a comprehensive framework for signal modeling and orientation estimation with multi-subcarrier transmissions, and the formulation of a maximum likelihood estimator (MLE). Moreover, we analyze the impact of imperfect tag location information, revealing that it minimally affects estimation accuracy. Exploiting related results, we propose an approximate MLE and introduce a low-complexity radiation pointing angle-based estimator with near-optimal performance. We derive the feasible orientation estimation region of the latter and show that it depends mainly on the system bandwidth. Our analytical results are validated through Monte Carlo simulations and reveal that the low-complexity estimator achieves near-optimal accuracy and that its feasible orientation estimation region is also approximately shared by the other estimators. Finally, we show that the optimal number of subcarriers increases with sensing time under a power budget constraint.

Index Terms—backscattering, LWA, MLE, orientation estimation, radar, RF sensing

I. INTRODUCTION

Accurate object orientation estimation is fundamental for efficient navigation, manipulation, interaction, alignment, and 3D vision in fields like robotics, aerospace, augmented reality, and medicine. Broadly speaking, orientation estimation may rely on local or external inference. *Local inference* is supported by embedding inertial measurement units, combining accelerometers, gyroscopes, and/or magnetometers, into the objects [1], [2]. Meanwhile, *external inference* shifts the complexity to an external system, using vision or radio frequency

O. López is with the Centre for Wireless Communications, University of Oulu, Finland, e-mail: onel.alcarazlopez@oulu.fi. Z. Han is with the Department of Electrical and Computer Engineering, University of Houston, Houston, Texas, USA, email: zhan2@central.uh.edu. A. Sabharwal is with the Department of Electrical and Computer Engineering, Rice University, Houston, Texas, USA, e-mail: ashu@rice.edu.

The work of O. López was partially supported by the Research Council of Finland (former Academy of Finland) 6G Flagship Programme (Grant Number: 346208), the KAUTE Foundation (*Tutkijat maailmalle* program), the Nokia Foundation (*Jorma Ollila* grant), the European Commission through the Horizon Europe/JU SNS project Hexa-X-II (Grant Agreement no. 101095759), and the Finnish-American Research & Innovation Accelerator. The work of Z. Han was partially supported by NSF CNS-2107216, CNS-2128368, CMMI-2222810, ECCS-2302469, US Department of Transportation, Toyota, Amazon, and Japan Science and Technology Agency (JST) Adopting Sustainable Partnerships for Innovative Research Ecosystem (ASPIRE) JPMJAP2326. The work of A. Sabharwal was partially supported by NSF Grants 1956297 and 2215082.

(RF) sensing modalities, responsible for solving the estimation problem. Each approach and specific techniques offer distinct advantages and challenges depending on the application context and the operational environment. Herein, we focus on RF sensing technology, which is especially appealing for cost-effective object orientation estimation [3]–[5].

The basic principle behind RF sensing is that the influence of the sensing targets on the reflected, refracted, and/or scattered wireless sensing signal can be potentially recognized [6]. Notably, one can enhance the RF-detectability and recognition of objects by engineering them. This can be achieved using advanced manufacturing (meta-)materials [7]–[9], attaching backscattering tags [9]–[18], and/or applying surface modifications [9] that interact with RF signals in predictable ways to passively (and indirectly) indicate object’s physical properties, as temperature, position, and orientation, the latter being the focus of the current work. This is akin to “painting an object” to be properly noticed by a camera [17], [18]. For example, incorporating metamaterials or antenna structures, applying conductive coatings, or attaching passive tags that can manipulate electromagnetic waves leads to more pronounced reflections or specific scattering patterns, thus making objects more distinguishable in complex environments. These approaches make objects smart and responsive without adding significant cost or weight.

In this work, we focus on a radar setup that aims to estimate the orientation of a backscattering tag. This tag can be on the surface of an object, and thus can be used to infer the object’s orientation and/or surface characteristics with low complexity.

A. Related Works

Passive RFID systems have been extensively exploited for orientation estimation applications, e.g., [10]–[18].¹ In general, they follow the idea of attaching passive RFID tags as orientation sensors on everyday objects. For instance, the data from multiple tags on carpets and peripherals is exploited in [10] for positioning and orientation estimation. Meanwhile, the authors in [11] designed phase sampling and recovery algorithms enabling reliable orientation sensing. Their experiments show the feasibility of the 3D orientation estimation of passive objects with an error as low as 4°. In [12], an RFID system for head orientation tracking was developed and shown to predict Euler angles with low error, thus suggesting potential for patient care and mobility aid solutions.

¹Although much less than for pure localization tasks. Readers interested in RFID-assisted localization may refer to [19]–[21] and references therein.

The proposals in [10]–[12] require conventional RFID systems with integrated circuits where tags encode some data, e.g., identification and relative position, motivating research on simpler (chipless) implementations to facilitate wider adoption. For instance, the framework in [13] can indeed estimate the inclination of objects tagged with chipless ultra-high frequency (UHF) tags. A simple statistical estimator based on the backscattered received signal strength (RSS) was derived for this and its good accuracy performance corroborated via experiments. Meanwhile, the authors in [14] exploited the cross-polar response of a periodic surface of a chipless RFID sensor with four dipoles for monitoring angular rotation at microwave frequencies. It was shown that the system can monitor rotation within a 180° span with up to 3° resolution, requiring a small bandwidth and a few reading frequencies. In [15], a chipless RFID system is proposed for accurately measuring the orientation of a tagged two-dimensional surface with less than 5° errors over a 90° range and unaffected by distance variations. Orientation is determined using analytical expressions from monostatic copolarization measurements, and verified with a practical implementation. An RFID array-based system is used in [16] for simultaneously estimating the position and orientation of a moving object exploiting differential sensing and the integration of the multiple signal classification (MUSIC) and hyperbolic positioning algorithms. An array of configurable backscatter tags is also exploited in [17], [18], in this case for estimating the 3D orientation of a tagged object. Therein, the authors design tag response codes to improve the orientation estimation accuracy.

The chipless RFID tags in [13]–[18] still store/encode some data. Also, polarization diversity or mismatch-based encoding techniques adopted in [13]–[15] are affected by distance, causing undesired RSS variations and limiting the sensing range. All these, together with the need for dual-polarized antennas [13]–[15] and multiple tags [16]–[18], complicate the system design and the data reading and interpretation process, and thus solution scalability. This calls for lower-complexity designs with purely passive, “dumb”, tags relying on their physical structure to interact with RF signals and thus avoiding chips, complex circuits, extensive calibration, and data storing and encoding capabilities.

B. Contributions and Organization of this Work

We hypothesize that ultra-low-complexity designs for object orientation estimation using RF sensing can be achieved by equipping the tags with beam-scanning antennas such as leaky-wave antennas (LWA)². The latter offer key advantages in beam steering, wide impedance bandwidth, high gain, low cost, easy fabrication, and compactness compared to other high-gain beam-steerable antennas such as phased array antennas [22]. Very importantly, the radiation pattern of an LWA can be synthesized using its (frequency-dependent) complex propagation constant. As a result, LWAs produce directive radiation beams that can be steered along one dimension

²LWAs radiate through the leakage of a traveling wave in a guiding structure. Please, refer to [22] for a comprehensive survey on their types, radiating features, and guiding structures, i.e., microstrip and waveguides.

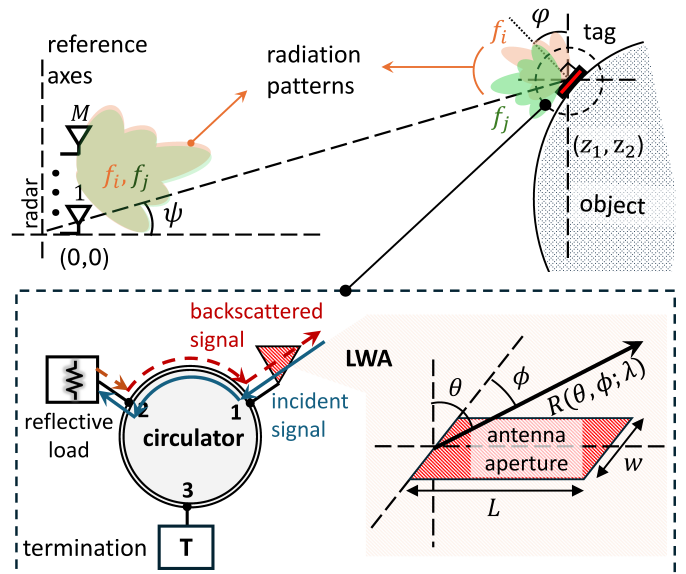


Fig. 1: A radar equipped with M full-duplex antennas interrogates an LWA-equipped *dumb* backscattering tag to infer latter’s orientation. We also depict a tag backscattering implementation, LWA geometry, and radiation angles.

by simply varying the operating frequency. In this work, we consider a radar aiming to estimate the orientation of an LWA-equipped backscattering tag as illustrated in Fig. 1. To the best of our knowledge, this is the first work of its kind in the literature. Our main contributions are three-fold:

1) *System design*: We propose an LWA-equipped tag design, and develop a comprehensive framework, encompassing system and signal modeling, for a radar system to sense its orientation using multi-subcarrier transmissions. With the latter, we leverage the LWA beam steering feature, i.e., each transmitted subcarrier experiences an LWA unique radiation pattern. Note that LWAs have been recently used in [23]–[27] for positioning-related tasks. However, these are posed as local inference problems, including direction-of-arrival (DoA) estimation, and thus require active circuitry at the tags. Instead, we propose incorporating a low-complexity backscattering circuit into the tag, e.g., using a circulator as illustrated in Fig. 1, shifting the object orientation estimation task to an external radar. We formulate the corresponding orientation estimation problem and discuss the associated challenges.

2) *Estimator formulation*: We formulate the maximum likelihood estimator (MLE) for the tag’s orientation, and its simplified form under perfect location information, referred to as P–MLE. The latter is derived to assess how such an estimator performs even under non-ideal tag location information availability. We formally assess the impact of the tag’s imperfect location information on the orientation estimation accuracy. In this regard, we demonstrate that the statistics of the tag’s location estimation errors do not influence the orientation estimation accuracy in practical deployments where the tag is relatively far from the radar. Specifically, as long as estimation errors are expected, their realizations do not greatly affect the orientation estimation accuracy. Based on these re-

sults and aiming for lower estimation complexity, we apply key simplifications to the MLE and attain an approximate MLE, referred to as A-MLE. Finally, we propose an additional simple tag radiation pointing angle-based estimator, referred to as RPA, that achieves near-optimal results. We derive the feasible orientation estimation region of RPA and show that it depends mainly on the system bandwidth. Moreover, we demonstrate that the estimation error vanishes asymptotically by increasing the number of subcarriers and estimation time.

3) *Performance and design insights:* We assess estimators' complexity and radar/tag implementation options, including simultaneous subcarrier and frequency-sweeping transmissions. The complexity of all the estimators is shown to scale with the product of the number of subcarriers and sampling time slots, but the number of radar antennas and brute force sampling points also increase significantly the complexity of A-MLE, P-MLE, and MLE compared to RPA. MLE even incurs the additional complexity of evaluating an expectation with respect to the tag location uncertainty. We corroborate our analytical insights and assess the performance of the proposed estimators via Monte Carlo simulations. It is shown that the feasible orientation estimation range obtained for RPA also applies to the other estimators. Moreover, A-MLE and RPA are shown to perform tightly close, outperforming P-MLE both in estimation accuracy under imperfect tag location information and complexity, and approaching MLE's accuracy with much lower complexity. We show there is an optimum number of subcarriers given a total power budget constraint, and that it increases with the sensing time.

The rest of this paper is organized as follows. Section II introduces the system model and tag orientation estimation problem while motivating a wideband design. The latter together with MLE and P-MLE are presented in Section III. Section IV characterizes the impact of the tag location information accuracy and presents A-MLE exploiting key related insights. The low-complexity estimator RPA is proposed in Section V, and performance trends are provided. Implementation considerations and numerical results are respectively discussed in Sections VI and VII. Section VIII concludes the article. Table I lists the main symbols used in the paper and their default values for performance analysis in Section VII.

II. SYSTEM SETTING

We consider the system illustrated in Fig. 1. Specifically, an array of M full-duplex antennas, i.e., capable of simultaneously transmitting and receiving in the same frequency band, illuminates a tag to infer its orientation angle with respect to the reference axes, assumed to be those of the radar antenna array. We focus on a 2D framework and analysis for simplicity, and thus assume a uniform linear radar array (ULRA). For convenience, but without loss of generality, we focus on the estimation of φ , hereinafter referred to as the orientation angle.

Let the ULRA consecutive antenna elements be spaced d meters apart, and set the position of the m -th element as $\mathbf{x}_m = [0, (m-1)d]^T$. Assume that the tag's location has been previously estimated, e.g., using state-of-the-art approaches as those described in [28]–[30]. We model this using

TABLE I: Main symbols utilized throughout the paper and their default values for performance assessment.

symbol	meaning	default value
M	number of radar antennas	4
$\varphi, \hat{\varphi}$	true, estimated orientation angle	—
d	consecutive radar antenna separation	$3 \times 10^8 / f_1$ (m)
\mathbf{x}_m	2D position of the m -th radar antenna	—
\mathbf{z}	true 2D position of the tag	$\ \mathbf{z}\ = 20$ m
$\hat{\mathbf{z}}, \Delta\mathbf{z}$	estimate and estimation error of \mathbf{z}	—
Σ	estimation error covariance matrix with diagonal entries σ_x^2 and σ_y^2	$\sigma_x = \sigma_y = \tilde{\sigma}$, $\tilde{\sigma} = 10$ cm
$\psi(\mathbf{z})$	polar angle of \mathbf{z}	—
k_z	complex propagation constant	—
θ	polar angle of the tag's radiation vector	—
ϕ	azimuth angle of the tag's radiation vector	$\pi/2$
F	number of transmit subcarriers	11
f_i	frequency of the i -th subcarrier	[34, 54] GHz
Δf	inter-frequency spacing	$20/(F-1)$ (GHz)
λ_i	wavelength of the i -th subcarrier	$3 \times 10^8 / f_i$ (m)
$R_i(\theta)$	radiation response the tag at frequency f_i and polar angle θ	given in App. A
s_i	complex radar signal transmitted at f_i	$\mathbf{E}[s_i ^2] = 1$
s'_i	complex signal impinging the tag at f_i	—
\tilde{s}'_i	noise-normalized signal received at the radar at f_i	—
$\mathbf{h}_i(\mathbf{z})$	channel vector between the radar and the spatial point \mathbf{z} at f_i	—
\mathbf{w}_i	power-normalized radar transmit precoder and receive combining vector at f_i	—
P_i	transmit power of subcarrier f_i	$\propto 1/F$
\tilde{n}_i	normalized complex noise at the radar	$\tilde{n}_i \sim \mathcal{CN}(0, 1)$
γ_i	transmit SNR of the i -th subcarrier	150 dB $-F$ (dB)
K	number of time samples	20
$\mathcal{L}(\varphi, \tilde{s}'')$	likelihood function of φ given \tilde{s}''	—
Φ	feasible search space for φ	—
N	number of points in a brute-force search	1000
Q	number of Monte Carlo samples for the exact estimator computation	100
$\theta_{0,i}$	main-lobe pointing angle of $R_i(\theta)$	(40) in App. A
$\Theta_i, \Theta(\lambda_i)$	half-power beamwidth of the main-lobe of $R_i(\theta)$	(42) in App. A
κ_i, u_i , v_i	relevant statistics for RPA computation related to the i -subcarrier	—
T_s	sampling period	4.63 ns
L, w	length, width of the LWA	5 cm, 1 cm

$$\hat{\mathbf{z}} = \mathbf{z} + \Delta\mathbf{z}, \quad (1)$$

where $\mathbf{z}, \hat{\mathbf{z}} \in \mathbb{R}^2$ are the true and estimated tag locations, respectively. Meanwhile, $\Delta\mathbf{z} \sim \mathcal{N}(\mathbf{0}, \Sigma)$ is the unbiased estimation error with co-variance matrix Σ . For simplicity, let each element of Σ be independently distributed, i.e., $\text{diag}(\Sigma) = [\sigma_x^2, \sigma_y^2]^T$. Note that the tag location angle with respect to the ULRA, denoted by ψ , is given by

$$\psi(\mathbf{z}) = \angle \mathbf{z} = \tan^{-1}(z_2/z_1). \quad (2)$$

Similarly, the estimated tag location angle is $\psi(\hat{\mathbf{z}})$.

A. LWA-equipped RF Sensor Tag

Assume a tag equipped with a LWA. Notably, the radiation pattern of an LWA can be synthesized through its complex propagation constant k_z , antenna geometry, and operation wavelength as exemplified in Appendix A.

Let θ and ϕ denote respectively a radiation vector's polar and azimuth angles from the spherical coordinate system, as illustrated in Fig. 1. Meanwhile, the complex radiation gain is

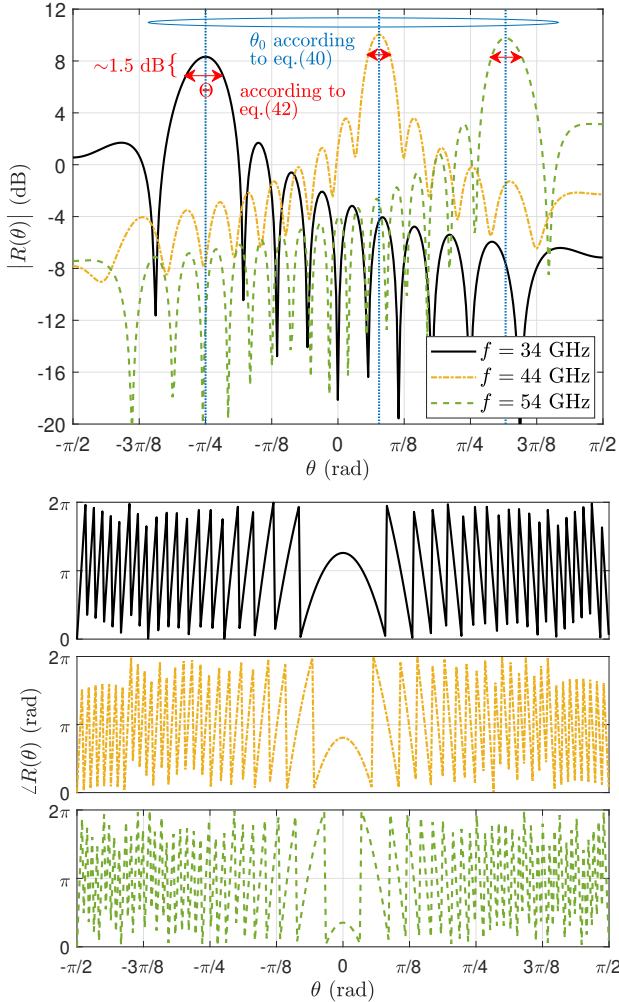


Fig. 2: a) Amplitude (top) and b) phase (bottom) radiation response of an LWA plotted according to the framework described in Appendix A.

denoted by $R(\theta, \phi; \lambda)$. Such a frequency-dependent radiation pattern is known in advance for a given LWA implementation. We assume that such a knowledge is perfect. Moreover, as we are focusing on a 2D analysis for simplicity, we can safely ignore the effect of the azimuth angle in our analyses. To simplify the notation, hereinafter we use $R(\theta)$ instead of $R(\theta, \phi; \lambda)$ assuming a given operation wavelength λ .

Fig. 2 illustrates the radiation pattern, both in terms of amplitude gain and phase response, for a given LWA mmWave implementation. Note that the radiation pattern varies indeed for different operation frequencies, being the more salient feature that the main-lobe pointing angle increases with the operation frequency.

B. Signal and Channel Model

Let s be a narrowband signal with unit average power, i.e., $\mathbb{E}[|s|^2] = 1$, transmitted by the ULRA towards the tag. Then, the signal impinging on the tag can be written as

$$s' = \sqrt{P} \mathbf{w}^H \mathbf{h}(\mathbf{z}) R(\theta(\varphi, \mathbf{z})), \quad (3)$$

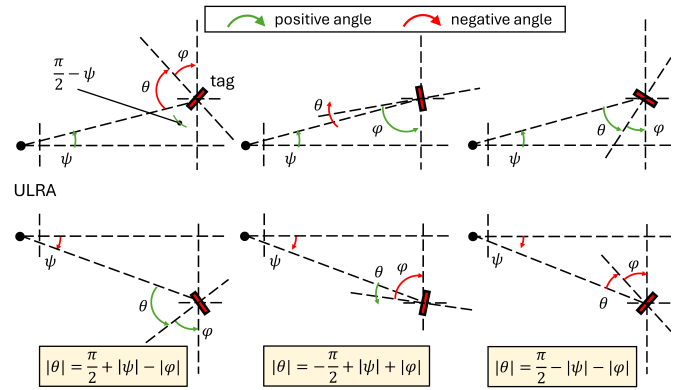


Fig. 3: The six possible setup geometries and corresponding equations. Angles signs are indicated with different colors according to the adopted convention.

where P is the transmit power, $\mathbf{h}(\mathbf{z}) = [h_1(\mathbf{z}), h_2(\mathbf{z}), \dots, h_M(\mathbf{z})]^T \in \mathbb{C}^M$ is the channel vector between the ULRA and the tag (at location \mathbf{z}), $\mathbf{w} \in \mathbb{C}^M$ is the power-normalized transmit precoder (and also receive combining) vector, i.e., $\|\mathbf{w}\|^2 = 1$. We consider free-space line-of-sight (LOS) conditions such that the channel between \mathbf{x}_m and $\mathbf{z} \in \mathbb{R}^2$ at frequency f is given by

$$h_m(\mathbf{z}) = \frac{\lambda}{4\pi \|\mathbf{x}_m - \mathbf{z}\|} \exp(-2\pi j \|\mathbf{x}_m - \mathbf{z}\|/\lambda), \quad (4)$$

where $\lambda = 0.3/f(\text{GHz})$ is the wavelength. Also, $\theta(\varphi, \mathbf{z})$ in (3) is the tag radiation polar angle experienced by the impinging signal. Note that this angle depends on the location and orientation of the tag relative to the ULRA. Fig. 3 illustrates this dependency for the six possible different cases. Assuming the sign conventions indicated in Fig. 3, which agree with (2) and Fig. 2, we can capture the angle mathematical models of the six cases with

$$\theta(\varphi, \mathbf{z}) = \text{sgn}(\varphi) \frac{\pi}{2} - \psi(\mathbf{z}) - \varphi, \quad (5)$$

where $\text{sgn}(\cdot)$ is the sign operator, i.e., $+/-1$ if the input is positive/negative. Moreover, from the left-most column cases in Fig. 3 and using geometry convention $|\theta| \leq \pi/2$, we have the following system constraint

$$\begin{cases} \psi(\mathbf{z}) + \varphi \leq 0, & \text{if } \psi(\mathbf{z}) > 0, \varphi < 0, \\ \psi(\mathbf{z}) + \varphi \geq 0, & \text{if } \psi(\mathbf{z}) < 0, \varphi > 0. \end{cases} \quad (6)$$

The tag backscatters the incident signal using a circulator and reflective load as discussed later in Section VI, while the reflected signal is then received at the ULRA. Considering perfect full-duplex self-interference cancellation,³ the signal received at the ULRA is given by

$$s'' = \mathbf{w}^H \mathbf{h}(\mathbf{z}) R(\theta(\varphi, \mathbf{z})) s' + n, \quad (7)$$

where n captures both the antenna noise at the tag and the antenna and signal processing noise at the ULRA. We model this noise as additive white Gaussian with variance σ^2 , i.e.,

³This can be nearly achieved in practical radar systems as transmit and receive arrays are notably separated [17], [31], [32].

$n \sim \mathcal{CN}(0, \sigma^2)$. Note that the noise at the ULRA dominates in practice. Substituting (1) and (3) into (7), we obtain

$$s'' = \sqrt{P}(\mathbf{w}^H \mathbf{h}(\hat{\mathbf{z}} - \Delta \mathbf{z}))^2 R(\theta(\varphi, \hat{\mathbf{z}} - \Delta \mathbf{z}))^2 s + n. \quad (8)$$

C. Goal and Challenges

Herein, we are concerned with finding an efficient estimator $\hat{\varphi} = g(s''|s, \hat{\mathbf{z}}, R(\cdot))$ for φ , where $g : \mathbb{C} \rightarrow [-\pi/2, \pi/2]$. Notably, estimating φ out of s'' faces some critical issues:

1) There are two randomness sources: n and $\Delta \mathbf{z}$. The impact of the former, and also the latter in case the tag location is simultaneously estimated with its orientation, can be mitigated in the time domain by taking enough samples of s'' as each would experience different noise realizations. However, if the latter is fixed for a given measurement setup as considered here, it introduces bias unresolvable in the time domain.

2) $R(\theta)$ is not monotonic on θ , but highly oscillatory, both in amplitude and phase, and thus creates unresolvable ambiguities⁴ even when $\Delta \mathbf{z} \rightarrow \mathbf{0}$ and $n \rightarrow 0$.

These call for further exploiting the frequency domain, e.g., using wideband transmissions as described next. Such an approach introduces measurement diversity to resolve $\Delta \mathbf{z}$. More importantly, the corresponding exploitation of the frequency scanning feature of LWAs allows radar signals to experience diverse radiation patterns, thus helping resolve ambiguities.

III. WIDEBAND DESIGN AND ESTIMATOR

Assume radar transmissions over F subcarriers. Without loss of generality, let them be equally spaced such that

$$f_i = f_1 + (i-1)\Delta f, \quad i = 1, 2, \dots, F, \quad (9)$$

denotes the i -th subcarrier, Δf is the inter-frequency spacing, and $F\Delta f$ is the system bandwidth. Compared to traditional radar waveforms, e.g., based on linear frequency modulation, such a frequency-division multiplexing is more flexible, adaptive, and easy to integrate with communication systems [33], although at the cost of increased susceptibility to certain interference and Doppler effects, potential high peak-to-average power ratio, and difficulties to solve range-Doppler ambiguity.

The analytical framework described previously is herein extended by including a subindex i to indicate the i -th subcarrier and $[k]$ to indicate the k -th time sample out of K . Specifically, we can rewrite (8) as

$$s''_i[k] = \sqrt{P_i}(\mathbf{w}_i^H \mathbf{h}_i(\hat{\mathbf{z}} - \Delta \mathbf{z}))^2 R_i(\theta(\varphi, \hat{\mathbf{z}} - \Delta \mathbf{z}))^2 s_i[k] + n_i[k], \quad (10)$$

for $i = 1, \dots, F$ and $k = 1, \dots, K$. The dependence of \mathbf{h}_i on the frequency is clear from (4).

After dividing both terms of (10) by σ , one obtains

$$\tilde{s}''_i[k] = \delta_i(\varphi, \Delta \mathbf{z}) s_i[k] + \tilde{n}_i[k], \quad \forall i, \forall k, \quad (11)$$

where $\tilde{s}''_i[k] = s''_i[k]/\sigma$, $\tilde{n}_i[k] = n_i[k]/\sigma \sim \mathcal{CN}(0, 1)$, and

$$\delta_i(\varphi, \Delta \mathbf{z}) \triangleq \sqrt{\gamma_i}(\mathbf{w}_i^H \mathbf{h}_i(\hat{\mathbf{z}} - \Delta \mathbf{z}))^2 R_i(\theta(\varphi, \hat{\mathbf{z}} - \Delta \mathbf{z}))^2 \quad (12)$$

with $\gamma_i \triangleq P_i/\sigma^2$ is the transmit signal-to-noise ratio (SNR) corresponding to the i -th subcarrier. Now note that for the

current setup, the radar should focus the sensing beam toward the expected position of the tag. Therefore, we adopt a maximum ratio transmit precoder, i.e.,

$$\mathbf{w}_i = \mathbf{h}_i(\hat{\mathbf{z}})/\|\mathbf{h}_i(\hat{\mathbf{z}})\|, \quad \forall i = 1, 2, \dots, F. \quad (13)$$

A. MLE

We rely on MLE to solve our problem. Since $\Delta \mathbf{z}$ is fixed and $\tilde{n}_i[k]$ realizations are independent over time and frequency-domain observations, $\tilde{s}''_i[k]$ samples are conditionally independent given $\Delta \mathbf{z}$ and $\tilde{n}_i[k]$. Therefore, the likelihood function $\mathcal{L}(\varphi; \tilde{\mathbf{s}})$ given the observed data $\{\tilde{s}''_i[k]\}$ can be written as

$$\begin{aligned} \mathcal{L}(\varphi; \tilde{\mathbf{s}}) &= \prod_{i=1}^F \prod_{k=1}^K \mathbb{E}_{\Delta \mathbf{z}} \left[p_{\tilde{s}''}(\tilde{s}''_i[k] \mid \varphi, \Delta \mathbf{z}) \right] \\ &\stackrel{(a)}{=} \prod_{i=1}^F \prod_{k=1}^K \mathbb{E}_{\Delta \mathbf{z}} \left[p_{\tilde{n}}(\tilde{s}''_i[k] - \delta_i(\varphi, \Delta \mathbf{z}) s_i[k] \mid \varphi, \Delta \mathbf{z}) \right] \\ &\stackrel{(b)}{=} \prod_{i=1}^F \prod_{k=1}^K \frac{1}{\pi} \mathbb{E}_{\Delta \mathbf{z}} \left[\exp \left(-(\tilde{s}''_i[k] - \delta_i(\varphi, \Delta \mathbf{z}) s_i[k])^H \right. \right. \\ &\quad \left. \left. \times (\tilde{s}''_i[k] - \delta_i(\varphi, \Delta \mathbf{z}) s_i[k]) \right) \right] \\ &\stackrel{(c)}{=} \prod_{i=1}^F \prod_{k=1}^K \frac{\exp(-|\tilde{s}''_i[k]|^2)}{\pi} \mathbb{E}_{\Delta \mathbf{z}} \left[\exp \left(-|s_i[k]|^2 \right. \right. \\ &\quad \left. \left. \times |\delta_i(\varphi, \Delta \mathbf{z})|^2 + 2\Re\{\tilde{s}''_i[k]^* s_i[k] \delta_i(\varphi, \Delta \mathbf{z})\} \right) \right], \quad (14) \end{aligned}$$

where (a) comes from using $\tilde{n}_i[k] = \tilde{s}''_i[k] - \delta_i(\varphi, \Delta \mathbf{z}) s_i[k]$ from (11), (b) from using the PDF of $\tilde{n}_i[k]$, which is a circularly symmetric complex normal random variable, and (c) from expanding the squared term inside the exponential function and isolating the non-random term outside the expectation. Then, the log-likelihood function for all observations over different frequencies and time slots is given by

$$\begin{aligned} \ln \mathcal{L}(\varphi; \tilde{\mathbf{s}}) &\propto \sum_{i=1}^F \sum_{k=1}^K \ln \mathbb{E}_{\Delta \mathbf{z}} \left[\exp \left(-|\delta_i(\varphi, \Delta \mathbf{z})|^2 |s_i[k]|^2 \right. \right. \\ &\quad \left. \left. + 2\Re\{\tilde{s}''_i[k]^* s_i[k] \delta_i(\varphi, \Delta \mathbf{z})\} \right) \right] \quad (15) \end{aligned}$$

after using $\ln \prod_i a_i = \sum_i \ln a_i$ and ignoring constant terms.

The MLE of the surface normal angle is given by

$$\hat{\varphi} = \arg \max_{\varphi \in \Phi} \ln \mathcal{L}(\varphi; \tilde{\mathbf{s}}), \quad (16)$$

where Φ is the feasible search space. Such a set comprises the whole $[-\pi/2, \pi/2]$ region excluding those intervals violating (6). Therefore, it can be written as

$$\Phi = \begin{cases} [-\pi/2, -\psi(\hat{\mathbf{z}})] \cup [0, \pi/2], & \text{if } \psi(\hat{\mathbf{z}}) > 0, \\ [-\pi/2, 0] \cup [-\psi(\hat{\mathbf{z}}), \pi/2], & \text{if } \psi(\hat{\mathbf{z}}) < 0. \end{cases} \quad (17)$$

Fig. 4 illustrates the log-likelihood function for ideal setups, that is assuming perfect tag location information and no noise impact. We can clearly observe function peaks at the ground-truth values of φ , while potential ambiguities arise in regions violating (6), but these can be easily discarded. Meanwhile, the other peaks in feasible regions arise due to the limited resolvability from a relatively small F . In fact, note that as F

⁴That is, several values of θ can produce the same $R(\theta)$.

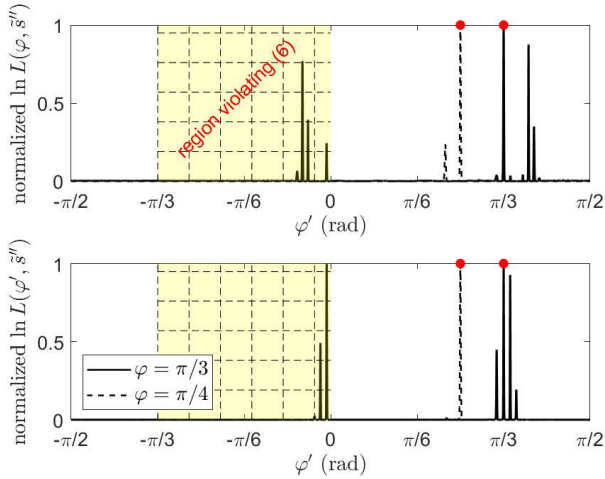


Fig. 4: Normalized log-likelihood function for a ground-truth $\varphi \in \{\pi/3, \pi/4\}$, $\psi = \pi/3$, and a) $F = 6$ (top) and b) $F = 16$ (bottom). We assume perfect position information, $\Sigma = \mathbf{0}$, and a noiseless (ideal) scenario, $\sigma^2 = 0$, while the remaining simulation parameters are those assumed by default in Section VII. The normalized values are obtained by applying the transformation: $(\cdot) \leftarrow ((\cdot) - \min(\cdot)) / (\max(\cdot) - \min(\cdot))$.

increases, the number high peaks at angles further from the ground truth φ decreases.

Unfortunately, there is no closed-form solution for (16). It is in fact intricate to compute the expectation of a highly non-linear function, which is required to evaluate (15).

B. MLE given Perfect Tag Location Information

Assume perfect tag location information. This is done with the hope of simplifying (16) and obtaining a low-complexity estimator that may be used even with non-perfect location information at the cost of reduced estimation accuracy. For this, let us substitute (15) into (16) while letting $\Delta \mathbf{z} \rightarrow \mathbf{0}$ such that we obtain the exact-position-based MLE (P-MLE)

$$\begin{aligned} \hat{\varphi} &= \arg \max_{\varphi \in \Phi} \sum_{i=1}^F \sum_{k=1}^K \left(2\Re\{\tilde{s}_i''[k]^* s_i[k] \delta_i'(\varphi)\} - |\delta_i'(\varphi)|^2 |s_i[k]|^2 \right) \\ &= \arg \max_{\varphi \in \Phi} \sum_{i=1}^F \left(2\Re\{u_i \delta_i'(\varphi)\} - |\delta_i'(\varphi)|^2 \right), \end{aligned} \quad (18)$$

where

$$u_i \triangleq \frac{1}{v_i} \sum_{k=1}^K \tilde{s}_i''[k]^* s_i[k], \quad v_i \triangleq \sum_{k=1}^K |s_i[k]|^2, \quad (19)$$

and $\delta_i'(\varphi) \triangleq \delta_i(\varphi, \mathbf{0})$, which according to (12) equals

$$\delta_i'(\varphi) = \sqrt{\gamma_i} \|\mathbf{h}_i(\hat{\mathbf{z}})\|^2 R_i(\theta(\varphi, \hat{\mathbf{z}}))^2. \quad (20)$$

Note that as per the signal model assumption at the beginning of Section II-B and by using a Nyquist sampling period, we have that $u_i \rightarrow \mathbb{E}[\tilde{s}_i''^* s_i]$ as $K \rightarrow \infty$.

C. Complexity Analysis

Computing (16) and (18) necessarily requires numerical optimization because i) the log-likelihood functions are highly non-linear and oscillatory, with many local peaks, due to the shape of $R_i(\theta)$ as illustrated in Fig. 2; and more importantly ii) $R_i(\theta)$ is unlikely to be given in closed-form in practice, but in tabulated form. Therefore, a brute-force search over $\varphi \in [-\pi/2, \pi/2]$ seems the only reasonable approach here, and affordable as we are dealing with a single-scalar estimator. The complexity of such optimization scales with the number of points to be evaluated within the interval, denoted by N , and the cost of evaluating the log-likelihood function. The choice of N depends on the desired optimization accuracy as the quantization error is given by $\pi/(N-1)$. For instance, if a resolution in the order of $1^\circ \rightarrow 0.017$ rad is required, then $N \geq \pi/0.017 + 1 = 185$. Meanwhile, the cost of evaluating the log-likelihood function comprises the computation of:

- the expectation of a highly non-linear function in (16). Monte Carlo-based integration is more appropriate here than other numeric integration approaches as $R_i(\theta)$ is likely in tabulated form. The corresponding complexity scales with the number of samples Q , while the integration error scales with $1/\sqrt{Q}$.
- M -dimensional vector multiplications within δ_i in (16) and δ_i' in (18). The corresponding cost increases linearly with M .
- sums over K , F , leading to $K \times, F \times$ increased complexity.
- scalar-valued functions, including $\exp(\cdot)$, $\ln(\cdot)$, $\Re\{\cdot\}$, $(\cdot)^2$, $\sqrt{\cdot}$, $(\cdot)^*$, $|\cdot|$, and scalar multiplication, which entail $\mathcal{O}(1)$.

Remark 1. Based on the above, the complexity of (16) and (18) is respectively given by $\mathcal{O}(NFKQM)$ and $\mathcal{O}(NFKM)$. Considering that Q must be large, the complexity of (18) is significantly reduced compared to (16). This comes, of course, with estimation performance degradation in practical setups, i.e., $\text{Tr}(\Sigma) > 0$, as discussed later in Section VII-A.

IV. DEGENERATIVE IMPACT OF TAG LOCATION INFORMATION INACCURACY

Imperfect location information, specified by $\Delta \mathbf{z}$, affects both channel estimation and the perceived radiation pattern of the tag for a given angular configuration. These are respectively captured by $\mathbf{w}_i^H \mathbf{h}_i(\hat{\mathbf{z}} - \Delta \mathbf{z})$ and $\psi(\hat{\mathbf{z}} - \Delta \mathbf{z})$. Herein, we approximately characterize their statistics for when estimation errors are much smaller than actual distance estimations, which constitutes the case of practical interest. In the sequence, this helps to quantify the degenerative impact of imperfect location information for normal angle estimation and to propose an approximate estimator to (16) with lower complexity.

A. Statistics of $\mathbf{w}_i^H \mathbf{h}_i(\hat{\mathbf{z}} - \Delta \mathbf{z})$ and $\psi(\hat{\mathbf{z}} - \Delta \mathbf{z})$

The following result reveals that channel estimation inaccuracy is approximately independent of the location estimation error statistics, i.e., Σ .

Lemma 1. $\mathbf{w}_i^H \mathbf{h}_i(\hat{\mathbf{z}} - \Delta \mathbf{z}) \sim \|\mathbf{h}_i(\hat{\mathbf{z}})\| \exp(jV)$, where V is uniformly random in $[0, 2\pi]$, as $\text{Tr}(\Sigma)/\|\hat{\mathbf{z}}\|^2 \rightarrow 0$ but $\text{Tr}(\Sigma) \neq 0$.

Proof. See Appendix B.

In a nutshell, the case of perfect location estimation, for which $\text{Tr}(\Sigma) = 0$, differs similarly from any other scenarios with imperfect location estimation, i.e., $\text{Tr}(\Sigma) \neq 0$. Indeed, the channel estimation inaccuracy does not increase, but remains statistically constant, with $\text{Tr}(\Sigma)$.

While Lemma 1 shows that the location estimation error statistics do not impact the channel estimation accuracy, the following result reveals that they do statistically affect the accuracy of the tag's angular position estimation.

Lemma 2. *As $\hat{z}_i/\sigma_j \rightarrow 0$, where $i \in \{1, 2\}$ and $j \in \{x, y\}$, the distribution of $\psi(\hat{\mathbf{z}} - \Delta\mathbf{z})$ converges to*

$$\mathcal{N}\left(\tan^{-1}\left(\frac{\hat{z}_2}{\hat{z}_1}\right), \frac{\sigma_x^2 \hat{z}_2^2 + \sigma_y^2 \hat{z}_1^2}{(\hat{z}_1^2 + \hat{z}_2^2)^2}\right). \quad (21)$$

Proof. See Appendix C.

Therefore, the tag's angular position estimate is unbiased and the estimation variance increases linearly with σ_x^2, σ_y^2 .

Remark 2. *Since $|\psi(\hat{\mathbf{z}} - \Delta\mathbf{z})| \leq \pi/2$, one can conclude that (21) is more accurate as $|\tan^{-1}(\hat{z}_2/\hat{z}_1)|$ is farther from $\pi/2$, i.e., when $\hat{z}_1 \ll \hat{z}_2$ and $\hat{z}_2 \ll \hat{z}_1$.*

As a corollary of Lemma 2, let $\sigma_x = \sigma_y = \tilde{\sigma}$, then $\psi(\hat{\mathbf{z}} - \Delta\mathbf{z}) \sim \mathcal{N}(\tan^{-1}(\hat{z}_2/\hat{z}_1), \tilde{\sigma}^2/|\hat{\mathbf{z}}|^2)$. This reveals more clearly how the angular estimation accuracy decreases with the squared distance between the ULRA and the tag.

Remark 3. *In many envisioned setups, $\tilde{\sigma}$ is on the order of ten/hundreds of centimeters, while $\|\mathbf{z}\|$, thus $\|\hat{\mathbf{z}}\|$, may vary from a few to hundreds of meters. Therefore, $\tilde{\sigma}/\|\hat{\mathbf{z}}\|$ is expected to be very small, and therefore, its effect may be negligible compared to the effect of the location estimation error on the channel estimation phase as characterized in Lemma 1.*

B. Approximate MLE (A-MLE) and Complexity Analysis

Results and insights from Lemma 1 and Lemma 2 can be exploited to achieve the following key result.

Theorem 1. *The MLE in (16) approximates to*

$$\arg \max_{\varphi \in \Phi} \sum_{i=1}^F \sum_{k=1}^K \left(I_0(2|\hat{s}_i''[k]||s_i[k]||\delta'_i(\varphi)) - |\delta'_i(\varphi)|^2 |s_i[k]|^2 \right), \quad (22)$$

when tag location estimation errors are much smaller, but with $\text{Tr}(\Sigma) \neq 0$, than the actual distance estimations. Herein, $I_0(\cdot)$ is the modified Bessel function of the first kind and order 0.

Proof. See Appendix D.

The estimator in (22) lacks the costly expectation operation in (16). However, it introduces the computation of $I_0(\cdot)$. Fortunately, for non-negative input values, $I_0(\cdot)$ can be easily and accurately approximated by a simpler function,⁵ thus avoiding incurring additional computation costs.

Remark 4. *Based on the above, we can conclude that the computational cost from using (22) scales as $\mathcal{O}(NFKM)$.*

⁵For instance, one can obtain via curve fitting $I_0(x) \approx 0.05x^{3.87} + 1$ for $0 \leq x \leq 5$, while $I_0(x) \approx 0.206 \times 2.6^x$ for $x \geq 5$. This provides an average relative absolute error inferior to 3%.

V. ULTRA-LOW-COMPLEXITY ESTIMATION

Note that computing (18), and even (22), although simpler than (16) with (15), still requires numeric optimization due to the highly non-linear/oscillatory behavior of the corresponding objective functions. Next, we propose a lower-complexity approach that addresses this issue and discuss its key features.

A. Tag Radiation Pointing Angle-based Estimator

Let $\theta_{0,i}$ be the main-lobe pointing angle of the radiation pattern corresponding to the i -th subcarrier,⁶ i.e.,

$$\theta_{0,i} \triangleq \arg \max_{\theta \in [-\frac{\pi}{2}, \frac{\pi}{2}]} |R_i(\theta)|. \quad (23)$$

Note that $\theta_{0,1} < \theta_{0,2} < \dots < \theta_{0,F}$, and assume

$$\theta_{0,1} - \Theta_1/2 \leq \theta(\varphi, \hat{\mathbf{z}}) \leq \theta_{0,F} + \Theta_F/2, \quad (24)$$

where Θ_i , equivalently represented as $\Theta(\lambda_i)$ in Appendix A, is the main-lobe half-power beamwidth of $|R_i|$. Then, by identifying the sub-carrier corresponding to the strongest backscattered signal, one may identify the main-lobe pointing angle, and with this, φ . For this, we must first estimate $|\delta'_i(\varphi)|$.

According to the results in Lemmas 1 and 2, the tag location information inaccuracy may be neglected here for practical setups, and thus we can focus on estimating $|\delta'_i(\varphi)|$. Interestingly, the MLE of $\delta'_i(\varphi)$ is u_i^* , being u_i given in (19). This comes from using classical results from estimation theory [34]. Meanwhile, $|u_i|$ can work as an estimator for $|\delta'_i(\varphi)|$. However, $|u_i|$ is, in general, a biased estimator of $|\delta'_i(\varphi)|$, tending to overestimate it, thus motivating the search for a more efficient estimator as given next.

Theorem 2. *An unbiased estimator for $|\delta'_i(\varphi)|$, denoted as $|\widehat{\delta'_i(\varphi)}|$, is obtained from solving*

$${}_1F_1(-1/2, 1, -|\delta'_i(\varphi)|^2 v_i) = 2|u_i| \sqrt{v_i/\pi}, \quad (25)$$

where ${}_1F_1(\cdot; \cdot; \cdot)$ denotes a confluent hypergeometric function of the first kind. For the low and high SNR asymptotic regimes, the corresponding estimators can be given respectively in closed form as follows

$$|\widehat{\delta'_i(\varphi)}| = \sqrt{4|u_i|/\sqrt{\pi v_i} - 2/v_i}, \quad (26)$$

$$|\widehat{\delta'_i(\varphi)}| = |u_i|. \quad (27)$$

Proof. See Appendix E.

Note that the high-SNR asymptotic estimator (27) matches the one coming from the absolute square transformation of the MLE of $\delta'_i(\varphi)$ as discussed before Theorem 2. Moreover, such an estimator is also valid as $K \rightarrow \infty$. Therefore, numeric solvers for (25) can exploit (27) as a good initial guess/point.

Remark 5. *Very importantly, since ${}_1F_1(-1/2, 1, -x) \geq 1$ for any $x \geq 0$, we have that solving (25) is feasible only when $2|u_i| \sqrt{v_i/\pi} \geq 1 \rightarrow |u_i| \geq \sqrt{\pi/v_i}/2$. In the case that $|u_i| < \sqrt{\pi/v_i}/2$, it is advisable to use the high-SNR expression, i.e., (27), as the low-SNR is also infeasible in such range. We adopt this approach when drawing numerical results in Section VII.*

⁶In Appendix A, we use the equivalent notation $\theta_0(\lambda_i)$.

Using (5), (20), and $|\varphi| \leq \pi/2$, we propose

$$\hat{\varphi} = \begin{cases} \pi/2 - \psi(\hat{\mathbf{z}}) - \theta_{0,i^*} & \text{if } -\psi(\hat{\mathbf{z}}) \leq \theta_{0,i^*} \leq \pi/2 - \psi(\hat{\mathbf{z}}) \\ -\pi/2 - \psi(\hat{\mathbf{z}}) - \theta_{0,i^*} & \text{if } -\pi/2 - \psi(\hat{\mathbf{z}}) \leq \theta_{0,i^*} \leq -\psi(\hat{\mathbf{z}}) \end{cases} \quad (28)$$

as a tag radiation pointing angle-based estimator, also referred to as RPA for brevity, where $i^* \triangleq \arg \max_i \kappa_i$, s.t., $-\pi/2 - \psi(\hat{\mathbf{z}}) \leq \theta_{0,i} \leq \pi/2 - \psi(\hat{\mathbf{z}})$, and

$$\kappa_i \triangleq \frac{|\widehat{\delta'_i(\varphi)}|}{\sqrt{\gamma_i} \|\mathbf{h}_i(\hat{\mathbf{z}})\|^2}. \quad (29)$$

Note that θ_{0,i^*} may diverge significantly from the ground truth θ due to the limited frequency diversity, i.e., relatively small F , causing a kind of quantization error, and/or due to a limited angular resolution, i.e., relatively large (small) $\theta_{0,1}$ ($\theta_{0,F}$) when $i^* = 1$ (F). We explore this further in the following.

Theorem 3. *The feasible estimation range for φ when using RPA is approximately given by*

$$\left[\text{sgn}(\varphi)\pi/2 - \psi(\hat{\mathbf{z}}) - \theta_{0,F} - \Theta_F/2, \right. \\ \left. \text{sgn}(\varphi)\pi/2 - \psi(\hat{\mathbf{z}}) - \theta_{0,1} + \Theta_1/2 \right]. \quad (30)$$

Proof. Let us depart from (28). Assume first that $-\psi(\hat{\mathbf{z}}) \leq \theta_{0,i^*} \leq \pi/2 - \psi(\hat{\mathbf{z}})$, then $\hat{\varphi} = \pi/2 - \psi(\hat{\mathbf{z}}) - \theta_{0,i^*} \geq 0$, and using the bounds in (24), one gets $\pi/2 - \psi(\hat{\mathbf{z}}) - \theta_{0,F} - \Theta_F/2 \leq \hat{\varphi} \leq \pi/2 - \psi(\hat{\mathbf{z}}) - \theta_{0,1} + \Theta_1/2$. Meanwhile, assuming $-\pi/2 - \psi(\hat{\mathbf{z}}) \leq \theta_{0,i^*} \leq -\psi(\hat{\mathbf{z}})$ in (28), one gets $\hat{\varphi} = -\pi/2 - \psi(\hat{\mathbf{z}}) - \theta_{0,i^*} \leq 0$. Using again the bounds in (24), one obtains $-\pi/2 - \psi(\hat{\mathbf{z}}) - \theta_{0,F} - \Theta_F/2 \leq \hat{\varphi} \leq -\pi/2 - \psi(\hat{\mathbf{z}}) - \theta_{0,1} + \Theta_1/2$ for this case. Combining these results, one achieves (30). \square

Remark 6. *By subtracting both bounds in (30), one obtains that the feasible angular estimation range is approximately given by $\theta_{0,F} - \theta_{0,1} + (\Theta_F - \Theta_1)/2$. Again, as the set of potential estimate values is discrete under RPA, we can expect a kind of quantization error that decreases proportional to F .*

B. Estimation Accuracy Performance Trends

The estimation dispersion of κ_i , as a measure of estimation inaccuracy, increases with that of $|u_i|$. The specific relationship between κ_i is quite involved as captured by (25), but much simpler in the asymptotic regimes as captured by (26) and (27). Specifically, κ_i increases with the square root and linearly with $|u_i|$ in the low and high-SNR regimes, respectively. In any case, the variance of $|u_i|$, which is characterized next, is useful as a measure of estimation dispersion of κ_i , matching the exact dispersion in the case of high-SNR.

Theorem 4. *The variance of $|u_i|$ is given by*

$$\mathbb{V}[|u_i|] = |\delta'_i(\varphi)|^2 + \frac{1}{v_i} \left(1 - \frac{\pi}{4} {}_1F_1 \left(-\frac{1}{2}, 1, -|\delta'_i(\varphi)|^2 v_i \right) \right), \quad (31)$$

which converges as K increases to

$$\mathbb{V}[|u_i|] = |\delta'_i(\varphi)|^2 + \frac{1 - \frac{1}{2} |\delta'_i(\varphi)| \sqrt{K\pi}}{K}. \quad (32)$$

Proof. From the distribution of $|u_i|$ given in Appendix E, we obtain (31). Since $v_i \rightarrow K \mathbb{E}[|s_i[k]|^2] \rightarrow K$ as $K \rightarrow \infty$, while using ${}_1F_1(-1/2, 1, x) \rightarrow 2\sqrt{-\frac{x}{\pi}}$ as $x \rightarrow -\infty$, we have

$${}_1F_1 \left(-\frac{1}{2}, 1, -|\delta'_i(\varphi)|^2 K \right) \rightarrow 2|\delta'_i(\varphi)| \sqrt{\frac{K}{\pi}} \text{ as } K \rightarrow \infty. \quad (33)$$

Substituting (33) into (31), we obtain (32). \square

Remark 7. *Note from (32) that $\lim_{K \rightarrow \infty} \mathbb{V}[|u_i|] = |\delta'_i(\varphi)|$, while $\lim_{F \rightarrow \infty} \mathbb{V}[|u_i|] = 1/K$ since $|\delta'_i(\varphi)| \propto \sqrt{\gamma_i}$ while γ_i decreases with F given a fixed total transmit power budget. Thus, arbitrarily increasing estimation accuracy requires increasing both F and K . Also, in high-SNR setups, using at least a large F seems compulsory.*

C. Complexity Analysis

The computational complexity of the estimator in (28) is $\mathcal{O}(F(K + C + M))$. This is because, for each subcarrier, one must compute $\sum_{k=1}^K |s_i[k]|$ and $|u_i|$, whose complexity scales with K , and then solve (25), assumed with complexity cost C , and evaluate (29), which requires computing the norm of an M -dimensional vector. Obtaining i^* and evaluating (28) incurs a complexity respectively of $\mathcal{O}(F)$ and $\mathcal{O}(1)$, thus negligible compared to the previous operations. In fact, $\theta_{0,i}$ specified in (23) is known in advance for any given tag.

Due to its quadratic convergence, the Newton-Raphson method is a natural conventional technique for efficiently solving (25). This method requires evaluating the confluent hypergeometric function and its derivative, each typically with complexity scaling with the number of terms N' , in their series expansion needed for the required precision. Meanwhile, given the quadratic convergence, the number of iterations required to achieve D digits of precision scales proportional to $\ln D$. Thus, the overall computational complexity scales as $C = N' \ln D$.

Since C from solving (25) can grow large for an arbitrary accuracy requirement, we alternatively propose

$$|\widehat{\delta'_i(\varphi)}| = \sqrt{\left(0.1944(|u_i| \sqrt{v_i/\pi} + 0.067)^2 - 1 \right)} / v_i \quad (34)$$

as a low-complexity closed-form approximate solution. This comes from using

$${}_1F_1(-1/2, 1, -x) \approx 1.134\sqrt{x+1} - 0.134, \text{ for } x \geq 0, \quad (35)$$

obtained via curve fitting. Via numerical analysis we found that the achieved fitting accuracy is noticeably good, with a relative approximation error always below 1.7%.

Remark 8. *The complexity of evaluating (35) only scales with K . Therefore, with its use, the estimator in (28) achieves a computational complexity of $\mathcal{O}(F(K + M))$, significantly lower than that of all the previous estimators.*

VI. IMPLEMENTATION CONSIDERATIONS

The backscattering tag can be realized by connecting the LWA to Port 1 of a circulator, a reflective load to Port 2, and a terminator to Port 3, as shown at the bottom of Fig. 1. The circulator directs the signal from the LWA at Port 1 to Port 2, where the reflective load reflects it back. The circulator then routes the reflected signal from Port 2 back to Port 1, allowing the LWA to reradiate it. Port 3 of the circulator is terminated with a matched load to absorb any unintended signals, preventing reflections and ensuring the integrity of the signal path. To fit this setup into a compact tag, the elements must be miniaturized and integrated efficiently. The

TABLE II: Estimators' acronyms & computational complexity

Estimator	Acronym	Complexity
exact MLE, (16)	MLE	$\mathcal{O}(NFKQM)$
exact-position-based MLE, (18)	P-MLE	$\mathcal{O}(NFKM)$
approximate MLE, (22)	A-MLE	$\mathcal{O}(NFKM)$
(based on) radiation pointing angle, (28)	RPA	$\mathcal{O}(F(K+M))$

LWA can be designed as a microstrip antenna on a printed circuit board (PCB). The circulator, which traditionally uses ferrite materials, can be implemented using modern integrated circuit technology or microstrip-based designs suitable for PCB integration [35], [36]. The reflective load can be a simple trace designed as an open or short circuit on the PCB. The termination at Port 3 can be a small surface-mount resistor that matches the system's characteristic impedance. These elements can be fabricated using standard PCB manufacturing techniques [35], ensuring a compact and low-cost implementation suitable for tag applications.

As per the signal processing techniques derived in Sections III-V to estimate the orientation of LWA-equipped tags, they are summarized in Table II together with their complexity. Independently of the specific estimator, there are two primary methods for transmitting the subcarriers:

1) *Simultaneous Transmissions*: This constitutes the approach considered in earlier sections. This requires the system to handle wideband transmissions, as multiple and widely-spaced frequencies are used concurrently. The main appeal of this approach is the short sensing time, which scales linearly with K , while the challenges are related to advanced hardware requirements, including a wideband full-duplex transceiver capable of generating, sending, and receiving without significant effective self-interference. This demands sophisticated filtering and separation techniques for mitigating intermodulation and cross-talk interference among subcarriers. The number of subcarriers F is limited as Δf cannot be smaller than the inverse of the sampling period, although this may not be a stringent limitation in systems with sufficiently large $f_F - f_1$.

2) *Frequency Sweeping Transmissions*: The subcarriers, formally carriers here, are transmitted in a time-division manner. The proposed signal processing techniques still apply, but they need to account for the sequential nature of the data collection. Indeed, the sensing time now scales linearly with KF , thus larger than for the simultaneous subcarrier transmissions approach, but the number of carriers F is not limited. Although the system can be now narrow-band, it must be capable of switching frequencies rapidly and accurately, while ensuring precise synchronization between transmission and reception times for each subcarrier. Still, the system design is simpler as it deals with one frequency at a time, reducing the complexity of signal processing and hardware requirements, making it more accessible for lower-cost implementations.

VII. NUMERICAL PERFORMANCE ANALYSIS

In this section, we numerically assess the performance of the derived estimators under practical system conditions. We show averaged results in terms of absolute estimation error,

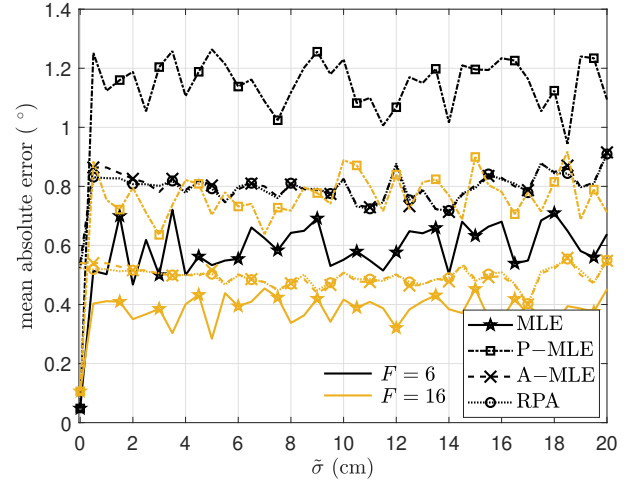


Fig. 5: Mean absolute estimation error of φ as a function of the standard deviation of the tag location estimation error for $F \in \{6, 16\}$, $\psi = 60^\circ$, and $\varphi = 30^\circ$.

i.e., $\mathbb{E}_{\hat{\mathbf{z}}}[\|\varphi - \hat{\varphi}(\hat{\mathbf{z}})\|]$, computed over 100 Monte Carlo system realizations. Results are given in degrees to ease interpretation.

The radiation profile of the LWA is computed according to the framework in Appendix A. Unless stated otherwise, we assume the system parameter values as indicated in the right-most column of Table I. Note that $f_1 = 34$ GHz and $f_F = 54$ GHz with $F \geq 2$, and $\Delta f = (f_F - f_1)/(F - 1)$, thus targeting a mmWave implementation.⁷ Moreover, we assume pure tone transmissions, i.e., without modulation (as this is not expected to bring any benefit according to the exposed framework), such that $s_i[k] = \exp(2\pi j f_i T_s (k - 1))$, where T_s is the sampling period. We set $T_s = 1/(4f_F) \approx 4.63$ ns. Also, let $P_i = P_T/F, \forall i$, where P_T is the total power budget, thus $\gamma_i = (P_T/\sigma^2)/F$, and we set $P_T/\sigma^2 = 150$ dB.⁸ Finally, we set $\tilde{\sigma} = 10$ cm as this is a well-known target for next-generation cellular-based positioning systems [28], [37].

A. Impact of Tag Location Estimation Error

Fig. 5 captures the mean absolute orientation estimation error as a function of $\tilde{\sigma}$ for $F \in \{6, 16\}$, $\psi = 60^\circ$, and $\varphi = 30^\circ$. The results here corroborate our findings in Section IV-A: the estimation performance is approximately independent of the location estimation error statistics, i.e., $\tilde{\sigma}$, for practical settings. The latter implies setups with imperfect tag location information and relatively small $\tilde{\sigma}/\|\mathbf{z}\|$. Indeed, note that MLE and P-MLE perform extremely well for $\tilde{\sigma} = 0$, but similarly worse for any other $\tilde{\sigma} > 0$. Meanwhile, since A-MLE exploits Lemma 1 assuming $\tilde{\sigma} > 0$, and RPA is agnostic of location estimation error statistics, they do not

⁷The considered 20 GHz system bandwidth may be $\sim 4 \times -5 \times$ the required by contemporary high-performance radars. Such a configuration is adopted here to realize a wide feasible angular estimation range. Notably, a smaller system bandwidth will reduce such a feasible angular estimation range while improving the estimation accuracy of the feasible angles. All this will become evident in the subsequent analysis.

⁸Assuming a pessimistically high subcarrier bandwidth for signal processing (after downconversion) of ~ 200 kHz, one would require $P_T \approx 1$ W to achieve this.

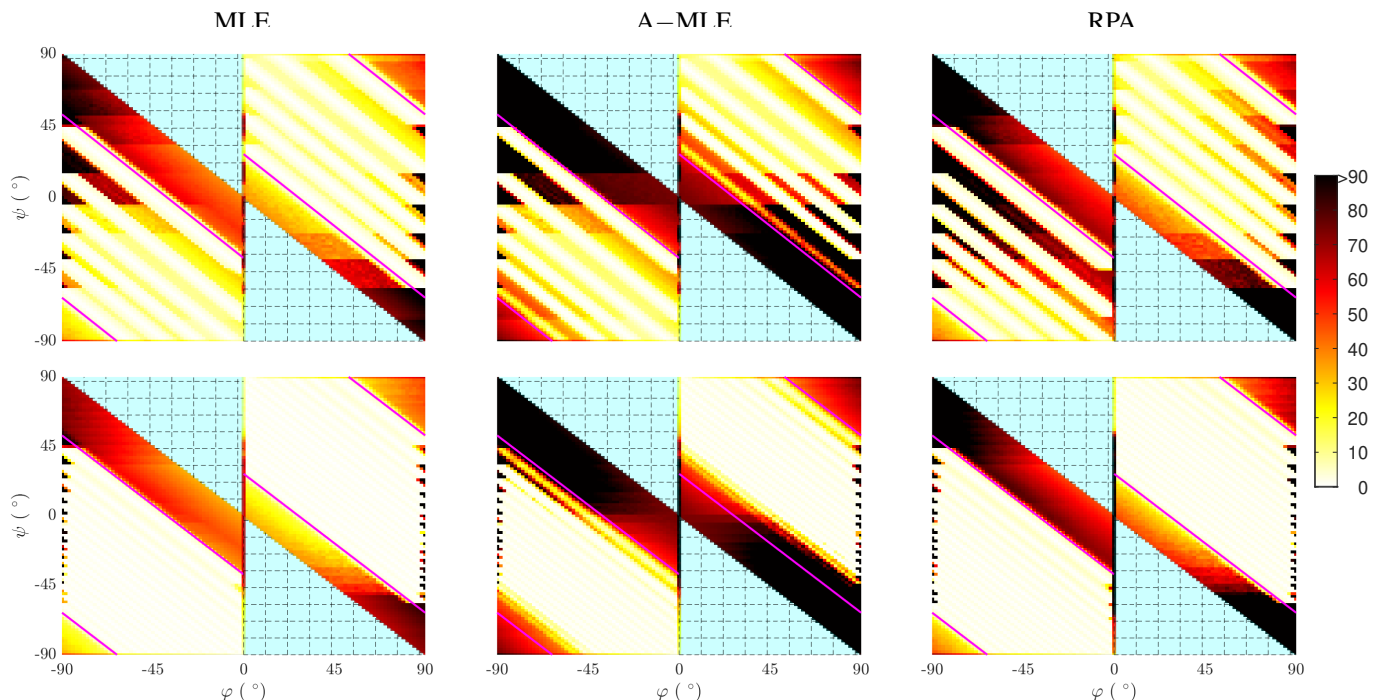


Fig. 6: Heatmap of the average mean estimation error of φ as a function of the tag angular position and target normal angle. We adopt $F = 6$ and $F = 16$ in the figures in the first and second rows, respectively. We illustrate with magenta lines the limits of the regions specified in (30), and color in a cyan pattern the (ambiguity) region violating (6).

offer as good performance for $\tilde{\sigma} = 0$. However, $\tilde{\sigma} = 0$ is not achievable in practice, tilting the scale in favor of A-MLE and RPA, which are more affordable. In fact, all the estimators perform similarly for $\tilde{\sigma} > 0$, although P-MLE does it relatively worse as it assumes no location estimation error and thus it does not exploit key related statistics, i.e., V in Lemma 1. We can observe that A-MLE and RPA perform tightly close and not far from MLE, evincing their robust design framework, especially that of RPA, which achieves this with extremely low complexity.

To facilitate discussions, we remove P-MLE from next numerical performance assessments. Recall that P-MLE underperforms all other estimators in any practical setting and with a complexity never lower than A-MLE and RPA.

B. On the Estimation Angular Range and Accuracy

Fig. 6 depicts the average mean estimation error of φ for all possible pairs (φ, ψ) and $F \in \{6, 16\}$. We color in cyan the (ambiguity) region violating (6), which can be discarded. Also, we illustrate with magenta lines the limits of the regions specified in (30), which notably apply accurately not only to RPA but also to MLE and less tightly to A-MLE. The latter suggests that the tag localization estimation error affects A-MLE more than RPA (and MLE, of course) in the boundary of (30). Indeed, it makes sense that the feasible estimation angular range for every estimator considered in this paper somewhat agrees with (30). This is because in such a region, every φ corresponds to a θ between $\theta_{0,1} - \Theta_1/2$ and $\theta_{0,F} + \Theta_F/2$, wherein all the pointing angles of the mainlobes of the LWA radiation pattern, $\{\theta_{0,i}\}$, reside. As shown

in Fig. 2a, there is no radiation amplitude ambiguity close to these pointing angles, thus accurately retrieving the ground-true θ (and then φ) is only possible here. In fact, the diagonal bright lines in Fig. 6 correspond to pairs (φ, ψ) that lead to θ values close to $\theta_{0,i}$ for some $i = 1, 2, \dots, F$. Note that the phase response of the LWA radiation pattern is expected with little, if any, impact on a proper estimator design due to no phase ambiguity-free region as illustrated in Fig. 2b. This is somewhat verified here also by noticing the similar performance attained by MLE, RPA, and A-MLE to some extent, being A-MLE and RPA only exploiting $\{R_i(\theta)\}$ -related information.

Regardless of the feasible angular estimation region's coverage, some angular configurations always cause poor estimator performance. That is the case of the (ψ, φ) pairs close to $(90^\circ, \pm 90^\circ)$, $(-90^\circ, \pm 90^\circ)$, $(\pm 45^\circ, \mp 45^\circ)$, and $(0^\circ, 0^\circ)$ since the signals impinging the tag arrive with $\theta \rightarrow \pm 90^\circ$. In addition to these, another critical configuration is that where $\varphi \approx -\psi(\hat{z})$ since a feasible/unfeasible angular configuration according to (6) may be identified as unfeasible/feasible due to tag localization estimation errors, thus affecting the whole orientation estimation process. Back to Fig. 6, observe that the feasible angular estimation regions light up as F increases from 6 to 16, as the number of bright lines matches $2F$ (F for each $\varphi > 0$ and $\varphi < 0$, each corresponding to a certain $\theta_{0,i}$), although not exactly in the case of A-MLE, as its accuracy is more affected in the boundary of the feasibility regions (30) as discussed earlier. In any case, an increase in F leads to better angular coverage in terms of estimation error. In fact, when computing the mean absolute estimation error of the lower 75-th percentile of the feasible angular estimation

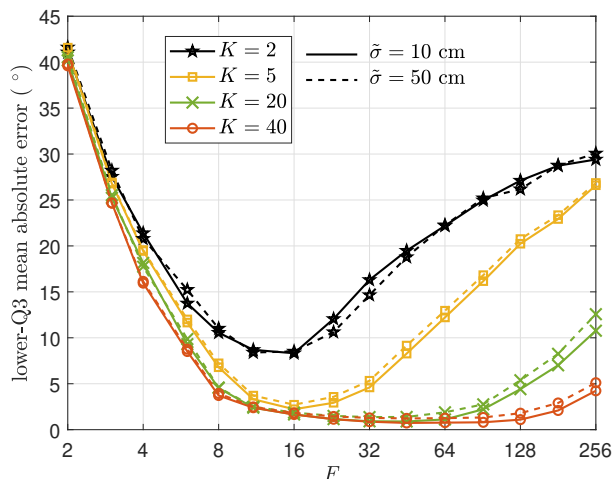


Fig. 7: Lower-Q3 mean absolute estimation error of φ as a function F for RPA with $K \in \{2, 5, 20\}$ and $\tilde{\sigma} \in \{10, 50\}$ cm. We compute the average performance over every φ within the feasible estimation range (30).

range, i.e., lower-Q3 mean, that is the mean estimation error for φ throughout the 75% best pairs (ψ, φ) in the so-called feasible angular estimation regions,⁹ we obtain values close to 3.6° , 8.8° , and 5.0° respectively for MLE, A–MLE, and RPA with $F = 6$, while these reduce to 0.9° , 2.1° , and 1.4° for $F = 16$. Note that a more homogeneous coverage can be achieved, at least for MLE and RPA, by selecting the subcarriers such that $\{\theta_{0,i}\}$ are equally spaced instead of using equally-spaced subcarriers as done here.

Next, we delve into angular coverage analysis while focusing only on the performance of RPA given its near-optimality and low complexity. This facilitates obtaining results even for a large F and having more focused illustrations and discussions.

C. Angular Coverage Accuracy

Fig. 7 shows the lower-Q3 mean absolute estimation error within the feasible angular estimation range (according to (30)) as a function of F , achieved by RPA for $K \in \{2, 5, 20, 40\}$ and $\tilde{\sigma} \in \{10, 50\}$ cm. The main highlight here is that given a fixed power and time budget, increasing F unbounded is not convenient as the transmit SNR of each subcarrier is increasingly affected and this can eventually deteriorate the estimation accuracy. This complements our insights in Remark 7. In fact, there is an optimum F , which increases with K . For example, for the setup simulated to draw Fig. 7, the optimum F is 12, 16, 45, and 52 for $K = 2$, $K = 5$, $K = 20$, and $K = 40$, respectively, leading to an orientation estimation error about 7.8° , 2.2° , 0.9° , and 0.7° . This can be explained by noting that each subcarrier transmission lasts longer by increasing K , which compensates for the reduced transmit SNR as F increases, i.e., effectively reducing sensing signal power but maintaining its energy. Remarkably, the tag location estimation error statistics do not affect much the orientation

⁹This is done to discard the effect of the outliers, including several angular configurations encompassing values of φ close to $\pm 90^\circ$.

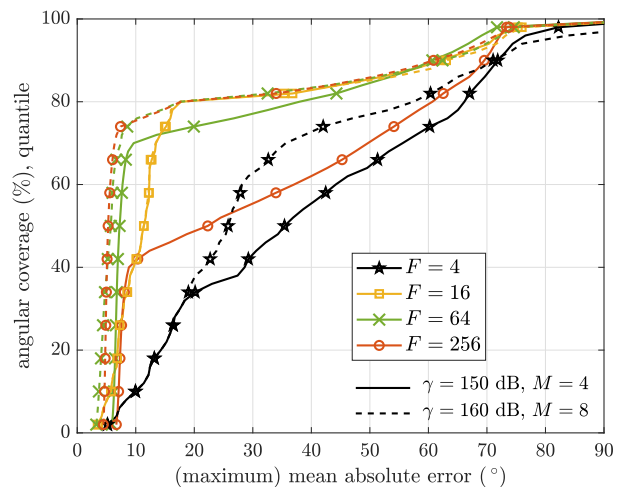


Fig. 8: Angular coverage (or quantile) achieved by RPA as a function of a target (maximum) mean absolute estimation error for φ , for $F \in \{4, 16, 64, 256\}$ and two (γ, M) configurations, namely $(150 \text{ dB}, 4)$ and $(160 \text{ dB}, 8)$. We assess this by considering φ in the feasible estimation range (30).

estimation accuracy and the optimum F , which agrees with our findings in Section IV-A.

Finally, Fig. 8 depicts the angular coverage achieved by RPA with respect to its feasible angular estimation range for a given target (maximum) mean absolute error for $F \in \{4, 16, 64, 256\}$ and two different configurations of (γ, M) . Note that as F increases the angular coverage may increase or decrease depending on the target accuracy as expected from our previous discussions around Fig. 7. Meanwhile, and as expected, a greater γ and/or M improves the estimation accuracy, and thus angular coverage given a target estimation accuracy. For instance, the maximum mean absolute estimation errors for a 60% angular coverage of the feasible estimation region can be approximately reduced 16° , 0° , 1.5° , and 31° for $F = 4, 16, 64$, and 256 , respectively, by increasing the transmit SNR in 10 dB and the number of antennas in 4.

VIII. CONCLUSIONS

In this work, we presented a novel RF sensing approach for accurate object orientation estimation using a *dumb* LWA-equipped backscattering tag within a radar system. Our framework includes comprehensive signal modeling, geometrical constraints assessment, and the development of several orientation estimators of varying complexity. Specifically, we formulated an MLE for the tag's orientation and its simplified form given perfect tag location information, namely P–MLE. In addition, we analyzed the effects of imperfect tag location information, and with related results derived A–MLE and RPA. Surprisingly, the magnitude of the tag location estimation error does not affect much the orientation estimation accuracy in practical settings. We derived the feasible orientation estimation region for RPA, and showed that it depends mainly on the system bandwidth and that it also applies approximately to the other estimators. Monte Carlo simulations corroborated our analytical insights and evinced that P–MLE is only

appealing given perfect tag location information, which is never available in practice. Meanwhile, they revealed that A–MLE and RPA perform near-optimally and achieve high accuracy given imperfect tag location information, the latter with significantly low complexity. Moreover, we showed that there is an optimum number of subcarriers given a power budget constraint, and that it increases with the sensing time.

It is worth noting that by leveraging LWAs' frequency-dependent radiation patterns, our method addresses key limitations of traditional orientation estimation techniques, offering a cost-effective and scalable solution suitable for various IoT applications. This is cornerstone for the widespread deployment of low-cost tags and sensors digitizing our society.

APPENDIX A LWA EXAMPLE RADIATION PATTERN

Let $k_z(\lambda) = \beta(\lambda) - j\alpha(\lambda)$, wherein α and β denote respectively the leakage rate and phase constant, and depend on the operation wavelength. For guided waves (such as those in microstrip lines or other types of transmission lines), for instance, β is determined by the effective refraction index n_{eff} of the mode of propagation, i.e., $\beta(\lambda) \approx 2\pi n_{\text{eff}}/\lambda$. Note that n_{eff} depends on the dielectric properties of the materials used in the construction of the transmission line or antenna structure and may vary slightly with frequency due to dispersion, i.e., the dependence of the dielectric constant on frequency. Meanwhile, α obeys

$$\alpha(\lambda) \approx \frac{2\pi\sqrt{\epsilon_{\text{eff}}}}{\lambda} \times \frac{\text{perturbation factor}(\lambda)}{\text{structural integrity}(\lambda)},$$

where ϵ_{eff} is the effective permittivity of the structure, while the perturbation factor captures how the design modifications, e.g., slots, cuts, or periodic structures, influence the guided wave, and the structural integrity captures how effectively the structure confines/guides electromagnetic waves, maintaining their propagation along the intended path within the antenna.

Assuming a grating LWA with antenna length L and width $w > \lambda$, as illustrated in Fig. 1, one has that $n_{\text{eff}} \approx \sqrt{\epsilon_{\text{eff}}}$ [38]. Also, for such a case, the far-field complex gain in the spatial direction determined by θ and ϕ is given by [38]

$$R(\theta, \phi; \lambda) = \sqrt{G(\lambda)S(\phi; \lambda)T(\theta, \phi; \lambda)} \exp(j\beta(\lambda)L \cos \theta), \quad (36)$$

where the directivity gain of the antenna, H -plane pattern, E -plane pattern, and main-lobe pointing angle are respectively given by

$$G(\lambda) = \frac{64w}{\alpha(\lambda)\pi} \tanh\left(\frac{\alpha(\lambda)L}{2}\right) \cos(\theta_0(\lambda)), \quad (37)$$

$$S(\phi; \lambda) = \sin^2 \phi \cos^2\left(\frac{\pi w}{\lambda} \cos \phi\right) \left(1 - \frac{4w^2}{\lambda^2} \cos^2 \phi\right)^{-2}, \quad (38)$$

$$T(\theta, \phi; \lambda) = \left(\frac{\alpha(\lambda)L}{1 - \exp(-\alpha(\lambda)L)}\right)^2 \left[1 - 2 \exp(-\alpha(\lambda)L)\right] \times \cos\left(\frac{2\pi L}{\lambda}(\sin \theta \sin \phi - \sin \theta_0(\lambda))\right) + \exp(-2\alpha(\lambda)L) \left/ \left(\alpha(\lambda)^2 L^2 + \frac{4\pi^2 L^2}{\lambda^2}(\sin \theta \sin \phi - \sin \theta_0(\lambda))^2\right), \quad (39)\right.$$

$$\theta_0(\lambda) = \sin^{-1}(n_{\text{eff}} - \lambda/d'). \quad (40)$$

Herein, d' is the grating period, which must be set to satisfy

$$\frac{\lambda}{n_{\text{eff}} + 1} \leq d' \leq \frac{\mu\lambda}{n_{\text{eff}} - 1}, \quad (41)$$

with $\mu = 1$ if $n_{\text{eff}} > 3$, otherwise $\mu = 2$. Meanwhile, the half-power beamwidth and radiation efficiency respectively satisfy

$$\Theta(\lambda) \approx \frac{\lambda}{L \cos(\theta_0(\lambda))}, \quad (42)$$

$$\eta(\lambda) = 1 - \exp(-2\alpha(\lambda)L). \quad (43)$$

At the design (pre-manufacturing) phase, the antenna geometry (e.g., L , w , d') and materials influencing α and β are selected according to the desired frequency-dependent radiation pattern [39]. Let's assume that the desired operation wavelength is in the range $[\lambda_{\text{min}}, \lambda_{\text{max}}]$. Then, from (41), one can select d' such that

$$\frac{\lambda_{\text{max}}}{n_{\text{eff}} + 1} \leq d' \leq \frac{2^{(\text{sgn}(3-n_{\text{eff}})+1)/2} \lambda_{\text{min}}}{n_{\text{eff}} - 1}, \quad (44)$$

while simultaneously considering the desired $\theta_0(\lambda)$, $\forall \lambda \in [\lambda_{\text{min}}, \lambda_{\text{max}}]$, according to (40). Then, one can set a target radiation efficiency η° , e.g., 90%, and then make the design according to (42) and such that

$$\alpha(\lambda)L \geq -\ln(1 - \eta^\circ)/2, \quad \forall \lambda \in [\lambda_{\text{min}}, \lambda_{\text{max}}], \quad (45)$$

which comes from (43).

Fig. 2 illustrates the radiation pattern, both in terms of amplitude gain and phase response, for a given LWA implementation using the framework described herein. Specifically, we adopt $L = 5$ cm, $w = 1$ cm, and target an operation frequency range of 34 – 54 GHz, corresponding to $\lambda \in [5.6, 8.8]$ mm. This allows using $\epsilon_{\text{eff}} = 12$ and $n_{\text{eff}} = \sqrt{\epsilon_{\text{eff}}}$ [38]. Moreover, we adopt $d' = 2.1$ mm, which lies in the middle of the feasible range characterized by (44). Finally, we use

$$\alpha(\lambda)\lambda = -\frac{0.36}{(\lambda_{\text{min}} - \lambda_{\text{max}})^2} \left(\lambda - \frac{\lambda_{\text{min}} + \lambda_{\text{max}}}{2}\right)^2 + 0.1 \quad (46)$$

to model the concave-quadratic behavior of $\alpha(\lambda)\lambda$ around the central operation wavelength as illustrated in [38, Fig. 11].

APPENDIX B PROOF OF LEMMA 1

Using (4), we have that

$$h_m(\hat{\mathbf{z}} - \Delta\mathbf{z}) = \frac{\lambda}{4\pi\|\hat{\mathbf{z}}'_m - \Delta\mathbf{z}\|} \exp\left(-\frac{2\pi}{\lambda}j\|\hat{\mathbf{z}}'_m - \Delta\mathbf{z}\|\right), \quad (47)$$

where $\hat{\mathbf{z}}'_m \triangleq \mathbf{x}_m - \hat{\mathbf{z}}$. Now, note that $\|\hat{\mathbf{z}}'_m\| \leq \|\hat{\mathbf{z}}'_m - \Delta\mathbf{z}\| \leq \|\hat{\mathbf{z}}'_m\| + \|\Delta\mathbf{z}\|$, and the bounds are tight for $\|\Delta\mathbf{z}\| \ll \|\hat{\mathbf{z}}'_m\|$, which is the case of practical interest. Indeed, we can safely ignore the effect of $\Delta\mathbf{z}$ on the path loss coefficient, but not that on the signal phase shift unless $\|\Delta\mathbf{z}\| \ll \lambda$ is guaranteed, which might only happen when using ultra-accurate positioning techniques, e.g., based on carrier phase measurements [37]. Hence, herein, we adopt the lower-bound of $\|\hat{\mathbf{z}}'_m - \Delta\mathbf{z}\|$ for the path loss component, and its upper-bound, capturing the

impact of $\Delta \mathbf{z}$, for the phase shift component. Then, (47) can be approximated as

$$\begin{aligned} h_m(\hat{\mathbf{z}} - \Delta \mathbf{z}) &\approx \frac{\lambda}{4\pi \|\hat{\mathbf{z}}'_m\|} \exp(-2\pi j(\|\hat{\mathbf{z}}'_m\| + \|\Delta \mathbf{z}\|)/\lambda) \\ &= h_m(\hat{\mathbf{z}}) \exp(-2\pi j\|\Delta \mathbf{z}\|/\lambda), \end{aligned} \quad (48)$$

thus, $\mathbf{h}_i(\hat{\mathbf{z}} - \Delta \mathbf{z}) \approx \mathbf{h}_i(\hat{\mathbf{z}}) \exp(-2\pi j\|\Delta \mathbf{z}\|/\lambda_i)$. Using this and (13), we obtain

$$\begin{aligned} \mathbf{w}_i^H \mathbf{h}_i(\hat{\mathbf{z}} - \Delta \mathbf{z}) &\approx \frac{\mathbf{h}_i(\hat{\mathbf{z}})^H}{\|\mathbf{h}_i(\hat{\mathbf{z}})\|} \mathbf{h}_i(\hat{\mathbf{z}}) \exp(-2\pi j\|\Delta \mathbf{z}\|/\lambda_i) \\ &= \|\mathbf{h}_i(\hat{\mathbf{z}})\| \exp(-2\pi j\|\Delta \mathbf{z}\|/\lambda_i). \end{aligned} \quad (49)$$

Now, since $\|\Delta \mathbf{z}\|$ has a continuous and unbounded distribution (as long as $\text{Tr}(\boldsymbol{\Sigma}) \neq 0$), we have that $\mathbf{w}_i^H \mathbf{h}_i(\hat{\mathbf{z}} - \Delta \mathbf{z}) \sim \|\mathbf{h}_i(\hat{\mathbf{z}})\| \exp(jV)$ with V is uniformly random in $[0, 2\pi]$ due to the wrapping effect of the phase about 2π . As per our previous discussions, this holds tight as $\text{Tr}(\boldsymbol{\Sigma})/\|\hat{\mathbf{z}}\|^2 \rightarrow 0$. \square

APPENDIX C PROOF OF LEMMA 2

We have $\psi(\hat{\mathbf{z}} - \Delta \mathbf{z}) = \tan^{-1}\left(\frac{\hat{z}_2 - \Delta z_2}{\hat{z}_1 - \Delta z_1}\right)$, where $\Delta z_1 \sim \sigma_x X$, $\Delta z_2 \sim \sigma_y Y$, and $X, Y \sim \mathcal{N}(0, 1)$. Let us put this with some notation abuse as $\psi(X, Y) = \tan^{-1}\left(\frac{\hat{z}_2 - \sigma_y Y}{\hat{z}_1 - \sigma_x X}\right)$. Since $\hat{z}_2, \hat{z}_1 \gg \sigma_y, \sigma_x$, a good approximation for this comes from its linear Taylor series approximation around $\mathbb{E}[X] = \mathbb{E}[Y] = 0$, for which the impact of σ_y, σ_x disappears. That is

$$\begin{aligned} \psi(X, Y) &\approx \psi(0, 0) + \left. \frac{\partial \psi(X, Y)}{\partial X} \right|_{(0,0)} X + \left. \frac{\partial \psi(X, Y)}{\partial Y} \right|_{(0,0)} Y \\ &= \tan^{-1}\left(\frac{\hat{z}_2}{\hat{z}_1}\right) + \frac{\sigma_x \hat{z}_2}{\hat{z}_1^2 + \hat{z}_2^2} Y - \frac{\sigma_y \hat{z}_1}{\hat{z}_1^2 + \hat{z}_2^2} X. \end{aligned} \quad (50)$$

Then, using the distribution of X and Y , we reach (21). \square

APPENDIX D PROOF OF THEOREM 1

When tag location estimation errors are much smaller than actual distance estimations, we can exploit the results and insights from Lemmas 1 and 2. Specifically, let us substitute $\mathbf{w}_i^H \mathbf{h}_i(\hat{\mathbf{z}} - \Delta \mathbf{z})$ by $\|\mathbf{h}_i(\hat{\mathbf{z}})\| \exp(jV)$ and $\psi(\hat{\mathbf{z}} - \Delta \mathbf{z})$ by $\psi(\hat{\mathbf{z}})$ into (15) to obtain

$$\begin{aligned} \ln L(\varphi; \tilde{s}'') &\propto \sum_{i=1}^F \sum_{k=1}^K \ln \mathbb{E}_V \left[\exp\left(-|\delta'_i(\varphi) \exp(jV)|^2 |s_i[k]|^2\right) \right. \\ &\quad \left. + 2\Re\left\{\tilde{s}''[k]^* s_i[k] \delta'_i(\varphi) \exp(jV)\right\}\right] \\ &= \sum_{i=1}^F \sum_{k=1}^K \left(\ln \mathbb{E}_V \left[\exp\left(2\Re\left\{\tilde{s}''[k]^* s_i[k] \delta'_i(\varphi)\right.\right.\right. \right. \\ &\quad \left. \left. \left. \times \exp(jV)\right\}\right) - |\delta'_i(\varphi)|^2 |s_i[k]|^2 \right), \end{aligned} \quad (51)$$

where the last line comes from exploiting $|a \exp(jV)| = |a|$, $\exp(a + b) = \exp(a) \exp(b)$, and $\ln \exp(a) = a$. Now, let $c =$

$2\tilde{s}''[k]^* s_i[k] \delta'_i(\varphi)$, so to proceed further we need to compute $E_V = \mathbb{E}_V[\exp(\Re\{c \exp(jV)\})]$ as pursued in the following

$$\begin{aligned} E_V &= \mathbb{E}_V \left[\exp\left(\Re\{\Re\{c\} + j\Im\{c\}\}(\cos V + j \sin V)\right)\right] \\ &\stackrel{(a)}{=} \mathbb{E}_V \left[\exp\left(\Re\{c\} \cos V - \Im\{c\} \sin V\right)\right] \\ &\stackrel{(b)}{=} \frac{1}{2\pi} \int_0^{2\pi} \exp\left(\Re\{c\} \cos v - \Im\{c\} \sin v\right) dv \stackrel{(c)}{=} I_0(|c|), \end{aligned} \quad (52)$$

where (a) comes from simple algebraic simplifications, (b) from using the PDF of V , given by $1/(2\pi), \forall v \in [0, 2\pi]$, to state the expectation in integral form, and (c) from exploiting [40, eq.(3.338.4)]. Finally, substituting (52) into (51) followed by some simple algebraic transformations, we obtain (22). \square

APPENDIX E PROOF OF THEOREM 2

Using the factorization theorem [34], u_i^* is a sufficient statistic for $\delta'_i(\varphi)$, and thus for $|\delta'_i(\varphi)|$. Note that $u_i^* \sim \mathcal{CN}(\delta'_i(\varphi), 1/\sum_{k=1}^K |s_i[k]|^2)$, thus $|u_i|$ follows a Rice distribution with parameters $|\delta'_i(\varphi)|$ and $(2 \sum_{k=1}^K |s_i[k]|^2)^{-1/2}$, and

$$\mathbb{E}[|u_i|] = \frac{1}{2} \sqrt{\frac{\pi}{\sum_{k=1}^K |s_i[k]|^2}} {}_1F_1\left(-\frac{1}{2}, 1, -|\delta'_i(\varphi)|^2 \sum_{k=1}^K |s_i[k]|^2\right). \quad (53)$$

Then, by substituting $\mathbb{E}[|u_i|]$ by $|u_i|$ in (53), thus, guaranteeing unbiased estimation, and performing some simple algebraic transformations, we obtain (25).

For asymptotically low and high SNR scenarios, i.e., $|\delta'_i(\varphi)| \rightarrow 0$ and $|\delta'_i(\varphi)| \rightarrow \infty$, we can exploit results from [41] to approximate ${}_1F_1(-1/2, 1, x) \rightarrow 1 - x/2$ as $x \rightarrow 0$, and ${}_1F_1(-1/2, 1, x) \rightarrow 2\sqrt{-\frac{x}{\pi}}$ as $x \rightarrow -\infty$. Substituting these into (25), we obtain (26) and (27). \square

REFERENCES

- [1] F. Mumuni and A. Mumuni, "Adaptive Kalman filter for MEMS IMU data fusion using enhanced covariance scaling," *Control Theory Technol.*, vol. 19, no. 3, pp. 365–374, Aug. 2021.
- [2] M. Benallegue *et al.*, "Velocity-aided IMU-based tilt and attitude estimation," *IEEE Trans. Automat.*, vol. 68, no. 10, pp. 5823–5836, Nov. 2023.
- [3] K. Klasing *et al.*, "Comparison of surface normal estimation methods for range sensing applications," in *IEEE ICRA*, May 2009, pp. 3206–3211.
- [4] O. Bialer *et al.*, "Object surface estimation from radar images," in *IEEE ICASSP*, May 2020, pp. 4132–4136.
- [5] M. Ulrich *et al.*, "Improved orientation estimation and detection with hybrid object detection networks for automotive radar," in *IEEE ITSC*, Oct. 2022, pp. 111–117.
- [6] P. Lee *et al.*, "Wireless sensing without sensors - an experimental approach," in *IEEE PIMRC*, Sep. 2009, pp. 62–66.
- [7] N. Kumar *et al.*, "A review on metamaterials for device applications," *Crystals*, vol. 11, no. 5, p. 518, May 2021.
- [8] W. Padilla and R. Averitt, "Imaging with metamaterials," *Nat. Rev. Phys.*, vol. 4, no. 2, pp. 85–100, Feb. 2022.
- [9] H. Xue *et al.*, "Radiofrequency sensing systems based on emerging two-dimensional materials and devices," *Int. J. Extreme Manuf.*, vol. 5, no. 3, p. 032010, Jul. 2023.
- [10] A. Shirehijini *et al.*, "An RFID-based position and orientation measurement system for mobile objects in intelligent environments," *IEEE Trans. Instrum. Meas.*, vol. 61, no. 6, pp. 1664–1675, Jun. 2012.
- [11] T. Wei and X. Zhang, "Gyro in the air: tracking 3D orientation of batteryless Internet-of-Things," in *Proc. MobiCom*, Oct. 2016, pp. 55–68.
- [12] G. Figueiredo *et al.*, "Monitoring head orientation using passive RFID tags," *IEEE J. Radio Freq. Identif.*, vol. 7, pp. 582–590, Oct. 2023.

- [13] R. Krigslund *et al.*, "Orientation sensing using multiple passive RFID tags," *IEEE Antennas Wirel. Propag. Lett.*, vol. 11, pp. 176–179, Jan. 2012.
- [14] S. Genovesi *et al.*, "Chipless radio frequency identification(RFID) sensor for angular rotation monitoring," *Technologies*, vol. 6, no. 3, p. 61, Jun. 2018.
- [15] N. Barbot *et al.*, "Angle sensor based on chipless RFID tag," *IEEE Antennas Wirel. Propag. Lett.*, vol. 19, no. 2, pp. 233–237, Nov. 2020.
- [16] H. Liu *et al.*, "Simultaneous detection of the orientation and position of moving objects with simple RFID array for industrial IoT applications," *IEEE Internet Things J.*, pp. 1–1, 2024.
- [17] K. Chang *et al.*, "'Wireless Paint': Code design for 3D orientation estimation with backscatter arrays," in *IEEE ISIT*, Jun. 2020, pp. 1224–1229.
- [18] M. Rammal *et al.*, "Coded estimation: Design of backscatter array codes for 3D orientation estimation," *IEEE Trans. Wirel. Commun.*, vol. 22, no. 9, pp. 5844–5854, Jan. 2023.
- [19] R. Anee and N. Karmakar, "Chipless RFID tag localization," *IEEE Trans. Microw. Theory Tech.*, vol. 61, no. 11, pp. 4008–4017, Oct. 2013.
- [20] W. Zhu *et al.*, "Fault-tolerant RFID reader localization based on passive RFID tags," *IEEE Trans. Parallel Distrib. Syst.*, vol. 25, no. 8, pp. 2065–2076, Aug. 2014.
- [21] G. Vougioukas and A. Bletsas, "DoA estimation with a single antenna and a few low-cost backscattering tags," *IEEE Trans. Commun.*, vol. 70, no. 10, pp. 6849–6860, Oct. 2022.
- [22] N. Javanbakht *et al.*, "A review of reconfigurable leaky-wave antennas," *IEEE Access*, vol. 9, pp. 94 224–94 238, Jun. 2021.
- [23] M. Poveda-García *et al.*, "Frequency-scanned leaky-wave antenna topologies for two-dimensional direction of arrival estimation in IoT wireless networks," in *EuCAP*, Mar. 2021, pp. 1–5.
- [24] A. Gil-Martínez *et al.*, "Direction finding of RFID tags in UHF band using a passive beam-scanning leaky-wave antenna," *IEEE J. Radio Freq. Identif.*, vol. 6, pp. 552–563, Jun. 2022.
- [25] —, "Frequency-scanned monopulse antenna for RSSI-based direction finding of UHF RFID tags," *IEEE Antennas Wirel. Propag. Lett.*, vol. 21, no. 1, pp. 158–162, Jan. 2022.
- [26] K. Neophytou *et al.*, "Simultaneous user localization and identification using leaky-wave antennas and backscattering communications," *IEEE Access*, vol. 10, pp. 37 097–37 108, Mar. 2022.
- [27] A. Gil-Martínez *et al.*, "Monopulse leaky wave antennas for RSSI-based direction finding in wireless local area networks," *IEEE Trans. Antennas Propag.*, vol. 71, no. 11, pp. 8602–8615, Nov. 2023.
- [28] C. de Lima *et al.*, "6G White Paper on localization and sensing," *6G Research Visions*, vol. 12, 2020.
- [29] M. Zhao *et al.*, "ULoc: low-power, scalable and cm-accurate UWB-Tag localization and tracking for indoor applications," *Proc. ACM IMWUT*, vol. 5, no. 3, Sep. 2021.
- [30] E. Soltanaghaei *et al.*, "Millimetro: mmWave retro-reflective tags for accurate, long range localization," in *Proc. MobiCom*. New York, NY, USA: ACM, Oct. 2021, p. 69–82.
- [31] K. Komatsu *et al.*, "Theoretical analysis of in-band full-duplex radios with parallel Hammerstein self-interference cancellers," *IEEE Trans. Wirel. Commun.*, vol. 20, no. 10, pp. 6772–6786, Oct. 2021.
- [32] Y. He *et al.*, "Frequency-domain successive cancellation of nonlinear self-interference with reduced complexity for full-duplex radios," *IEEE Trans. Commun.*, vol. 70, no. 4, pp. 2678–2690, Apr. 2022.
- [33] C. Ozkaptan *et al.*, "OFDM pilot-based radar for joint vehicular communication and radar systems," in *IEEE VNC*, 2018, pp. 1–8.
- [34] S. M. Kay, *Fundamentals of statistical signal processing: estimation theory, Volume i*. Prentice-Hall, Inc., 1993.
- [35] Z. Feng *et al.*, "Performance improvement of embedded microstrip circulators in printed circuit board," in *IEEE APMC*, Nov. 2017, pp. 525–528.
- [36] Y. Cui *et al.*, "Monolithic integration of self-biased C -band circulator on SiC substrate for GaN MMIC applications," *IEEE Electron Device Lett.*, vol. 40, no. 8, pp. 1249–1252, Aug. 2019.
- [37] O. López *et al.*, "Polarization diversity-enabled LOS/NLOS identification via carrier phase measurements," *IEEE Trans. Commun.*, vol. 71, no. 3, pp. 1678–1690, Mar. 2023.
- [38] F. Schwering and S. Peng, "Design of dielectric grating antennas for millimeter-wave applications," *IEEE Trans. Microw. Theory Tech.*, vol. 31, no. 2, pp. 199–209, Feb. 1983.
- [39] A. Oliner *et al.*, "Leaky-wave antennas," *Antenna engineering handbook*, vol. 4, p. 12, 2007.
- [40] I. Gradshteyn and I. Ryzhik, *Table of integrals, series, and products*. Academic press, 2014.
- [41] F. Olver *et al.*, *NIST handbook of mathematical functions hardback and CD-ROM*. Cambridge university press, 2010.